ARTICLE

# Developing Post-Modified Ce-MOF as Photocatalyst: A Detail Mechanistic insight of $CO_2$ Reduction towards Selective C2 Product Formation

Received 00th January 20xx,
Accepted 00th January 20xx

DOI: 10.1039/x0xx00000x

Sanchita Karmakar [a], Soumitra Barman [a], Faruk Ahamed Rahimi [a], Sandip Biswas [a], Sukhendu Nath[b] and Tapas Kumar Maji*[a]

Visible light-driven C-C bond formation to produce C2-based liquid fuel selectively from $CO_2$ is of great interest and remains a challenging task due to uphill electron transfer kinetics. Herein, we have developed $[Ru(bpy)_2]^{2+}$ grafted UiO-66-bpydc **Ce-MOF** via post-synthetic modification to harvest visible light based on MLCT ($Ru^{II}_{d\pi} \rightarrow \pi^*_{bpy}$) transition. The employment of Ru-grafted **Ce-MOF** facilitates fast electron transfer due to the vacant low-lying 4f orbital of $Ce^{IV}$, which was realized from ultrafast transient absorption (TA) spectroscopy, XANES and *in-situ* UV-vis spectroscopy. The synergistic effect of facile electron transfer and concomitant accommodation of two $CO_2$ molecules in proximal defect-site in $Ce^{IV}$ leads to facile C-C bond formation via COOH* coupling to yield acetic acid. The catalytic assembly produces 1133 µmol $g^{-1}$ of acetic acid with an impressive rate of 128 µmol $g^{-1}$ $h^{-1}$ suppressing the formation of other C1-based carbonaceous products in water (with selectivity 99.5%, Apparent Quantum Yield (AQY) = 0.93%). A detailed DFT calculation has been performed to understand the mechanistic pathway of C-C bond formation, and the generation of different surface-adsorbed intermediates was further supported by the *In-situ* Diffuse Reflectance Infrared Fourier Transform Spectroscopic (DRIFT) study.

## Introduction

Empowering photochemical reduction of $CO_2$ into multi-carbon chemicals and liquid fuels using water as the proton supplier can store intermittent solar light as chemical energy while mitigating $CO_2$ concentration in the atmosphere.[1-5] Despite significant advancement, the rational development of photocatalysts that can convert $CO_2$ into specific products at a fair production rate is limited to C1-based products such as HCOOH, CO, $CH_3OH$, and $CH_4$. Considering the energy-rich $CO_2$-reduced products, C2-based feedstocks such as acetic acid, ethanol, ethylene, and other hydrocarbons have high global market value due to their high energy density than the C1-based products.[6] In principle, the sluggish $CO_2$ activation kinetics, transfer of multiple electrons and protons and the C-C bond formation are the major hurdles to overcome for C2 product formation.[4] Thus, photocatalytic $CO_2$ reduction to a particular C2 product is nontrivial as a high density of photogenerated electrons and an increased charge accumulation near the catalytic site are essential. In this context, the rational development of efficient photocatalysts for C2-based product formation by boosting the electron density near the catalytic site to enhance the C2 selectivity avoiding C1 product formation is still remained an elusive task to accomplish. Among the C2 products, the demand for acetic acid caught significant attention due to the increased demand for ethyl acetate monomer from the adhesives and sealants industry. The versatile utilization of acetic acid in textiles, automobiles, construction, and food additives is also noteworthy. In this context, continuous efforts are being devoted for developing efficient photocatalyst which can trigger C-C bond formation in photochemical $CO_2$ reduction.

Recent progress on metal-organic frameworks (MOFs) with metallic nodes and tailorable organic linkers enlightens the path of photocatalysis, including hydrogen evolution by water splitting and $CO_2$ reduction reaction ($CO_2RR$). The MOFs as photocatalysts for $CO_2RR$ stems from its structural tunability by the introduction of suitable redox-active metal nodes or organic linkers and the capability of post-synthetic modification by light-harvesting moiety and catalytic centre.[7, 8] Further, the permanent porosity of MOFs allows the facile diffusion of $CO_2$ towards active catalytic sites in the framework. Although several MOF-based $CO_2$ photocatalysts are reported, those are mainly limited to C1-based product formation, and the utilization for generation of C2-based products is hardly explored.[2] In fact, two adjacent active $CO_2$ binding sites enhance the possibility of generating

[a] *Molecular Materials Laboratory, Chemistry and Physics of Material Unit (CPMU), School of Advance Material (SAMat), Chemistry and Physics of Materials Unit, Jawaharlal Nehru Centre for Advanced Scientific Research,Jakkur, Bangalore-560064 (India), E-mail: tmaji@jncasr.ac.in, Tel: +91 80 220282826*

[b] *Radiation & Photochemistry Division, Bhabha Atomic Research Centre, Maharashtra, 400085 (India)*

Electronic Supplementary Information (ESI) available: [details of any supplementary information available should be included here]. See DOI: 10.1039/x0xx00000x

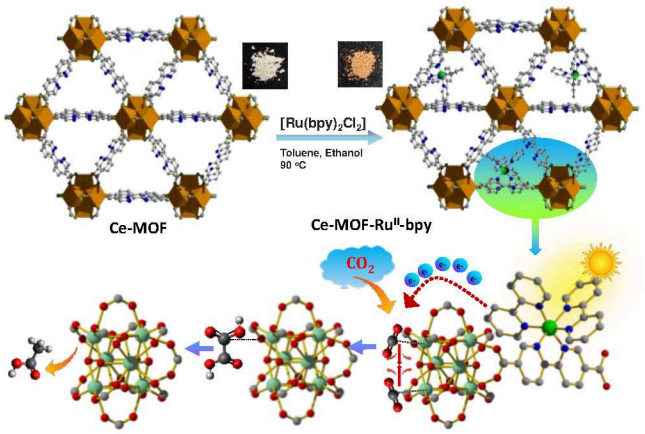


**Scheme 1**. Schematic for the construction of **Ce-MOF-Ru$^{II}$-bpy** and photochemical $CO_2$ reduction through **Ce-MOF-Ru$^{II}$-bpy** under visible light irradiation in pure water.

C2-based product during photochemical $CO_2$RR via C-C bond formation.[4] Very recently, exploration of Cerium (Ce)-based MOFs as photocatalyst caught considerable attention mainly due to the presence of low lying vacant f-orbital of $Ce^{IV}$, which intends to facilitate low energy linker to metal charge transfer (LMCT) in the visible light.[9] Moreover, the facile ligand to metal charge transfer (LMCT) and spontaneously flip-flop $Ce^{IV}/Ce^{III}$ redox recycling in **Ce-MOFs** could accelerate electron injection into the SBU node to generate $Ce^{III}$ active sites, which can reduce $CO_2$ efficiently.[10-16] Additionally, the nanoscale metal-organic framework is highly desirable for catalytic reactions due to the presence of high density catalytic sites per unit area, and also can be well dispersed in aqueous or any other medium.[17] In addition, the presence of linker-defect can create unsaturated active metal centers in the inorganic SBU and act as active $CO_2$ binding site which in turn would be beneficial for the formation of C-C bond. Thus, we envisioned that the linker defect-based Ce UiO-66 MOF could be a potential photocatalyst for C2-based product generation as such MOF can provide two proximal unsaturated Ce(IV) sites for $CO_2$ binding.[18] However, one of the major drawbacks of employing these MOFs as photocatalysts is the lack of sufficient visible light-harvesting capacity, which limits them from developing artificial photosynthetic systems. Considering this hurdle, we envisaged the catalyst design by introducing visible light harvesting moiety by post-synthetic modification in a Ce-MOF.

Herein, UiO-66 (Ce)-MOF has been chosen as the platform for post-synthetic modification due to its exceptional chemical, mechanical, and thermal stabilities. Bipyridine dicarboxylate (bpydc) linker was utilized during the synthesis of UiO-66 (Ce) to anchor $[Ru(bpy)_2Cl_2]$ post-synthetically as a light-harvesting unit to utilize visible light from the solar spectrum. The catalytic assembly was able to produce acetic acid as a $CO_2$ reduction product by boosting C-C bond formation. The catalytic efficiency and selectivity for acetic acid production are significantly higher as compared to the only handful of reported photocatalytic systems for $CO_2$ reduction.[2-4] The synergistic effect of facile charge transfer from Ru-bpy photosensitizer to low-lying vacant f-orbital results in C-C bond formation to produce acetic acid selectively. **Ce-MOF-Ru$^{II}$-bpy** produced 1133 µmol $g^{-1}$ of $CH_3COOH$ with 99.5% selectivity in aqueous medium, suppressing other C1-based reduced products along with $H_2$ evolution. To the best of our knowledge, this is the highest yield towards $CH_3COOH$ formation. [2-4] Ultra-fast transient absorption (TA) spectroscopy revealed the fast electron transfer from the $[Ru(bpydc)(bpy)_2]^{2+}$ (PS) moiety to the low-lying LUMO of the Ce-oxo cluster. Furthermore, reaction intermediates responsible for facilitating C-C bond formation were identified through *in situ* DRIFT, *in situ* UV-vis spectroscopy and DFT calculation.

## Results and discussion

The UiO-66 analogue $[Ce_6(\mu_3\text{-}O)_4(\mu_3\text{-}OH)_4(bpydc)_6]$ [bpydc=2,2′-Bipyridine-5,5′-dicarboxylate] (**Ce-MOF**) has been synthesized using $H_2$bpydc and cerium(IV) ammonium nitrate as reported earlier.[19] The structure is constructed with $[Ce_6(\mu_3\text{-}O)_4(\mu_3\text{-}OH)_4]^{12+}$ clusters and bpydc linkers in a cubic close-packed arrangement (Scheme 1).[19] The clusters are connected to form 3D porous frameworks with **fcu** topology, consisting of octahedral and tetrahedral cages with an internal pore diameter of 1.4 nm and 1.1 nm, respectively (Fig. S1). The UiO-66 structure of **Ce-MOF** was confirmed by a powder X-ray diffraction study (PXRD) (Fig. 1a). Furthermore, Le Bail refinement was carried out on the lattice parameters to confirm phase purity. The result suggested **Ce-MOF** is isostructural to previously reported Ce-UiO-66-bpydc MOF, which crystallized in a space group of $Fm\bar{3}m$ with a lattice parameter of $a = b = c = 27.3195$ Å and $\alpha = \beta = \gamma = 90°$ (Fig. S2).[19] TEM and FESEM measurements of **Ce-MOF** showed cubic morphology with diameters in the range of 100-150 nm (Fig. S3,S4). Notably, **Ce-MOF** exhibited lattice fringes with an interplanar distance of 1.4 nm, which is corresponds to the pore size of the pristine **Ce-MOF**. The FTIR spectra of **Ce-MOF** depicted the peaks at 1589 $cm^{-1}$ and 1400 $cm^{-1}$ were attributed to the asymmetric and symmetric stretching vibration of O-C-O of bpydc linker (Fig. S5).[20] In addition, a low-intensity band near 500-700 $cm^{-1}$ was also observed due to Ce-O stretching vibration.[21] Thermogravimetric analysis-Mass Spectrometry (TGA-MS) studies were performed under $N_2$ atmosphere to understand thermal stability and the fragment formed upon framework collapse (Fig. S6). The desolvated framework of **Ce-MOF** is stable up to 300 °C. Further, increment of the temperature from 300 to 550 °C, a significant weight loss was observed, and the corresponding mass spectra comprised m/z values of 44, 45, 77, 154, and 244, which are the cracking residue of the bpydc linker. So, the weight loss observed for the bpydc linkers per formula unit is about 44.08 %, which is less than the calculated value (52.92%). Therefore, TGA-MS result suggested that as-synthesized **Ce-MOF** comprised of the structural defect arising from one missing bpydc linker. Hence, the Ce-oxo cluster is connected with five bpydc linkers instead of six, with the framework formula of

ARTICLE

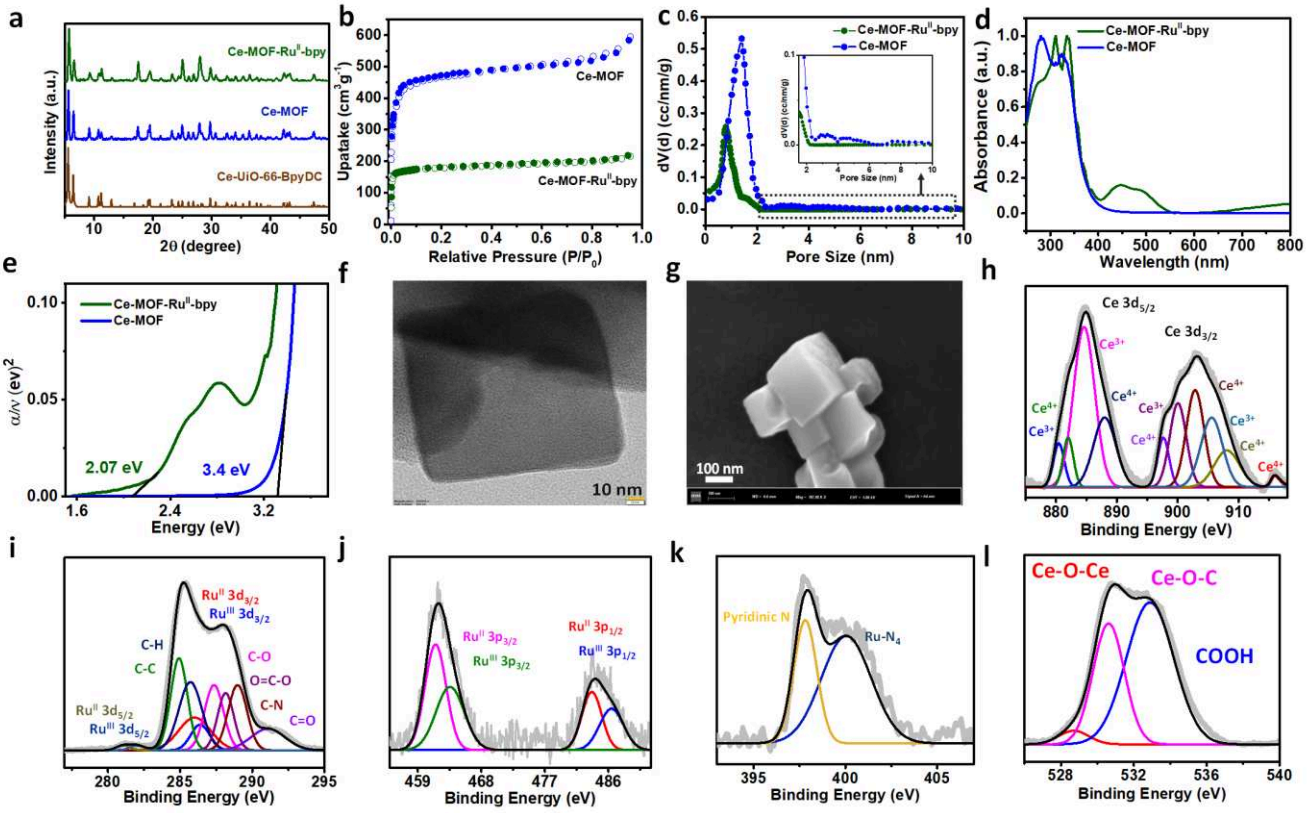


**Fig. 1** Characterization and illustration of **Ce-MOF** and **Ce-MOF-Ru$^{II}$-bpy.** (a) PXRD pattern of **Ce-MOF** and **Ce-MOF-Ru$^{II}$-bpy** compared with the simulated pattern calculated from the single-crystal structure of Ce-UiO-66-bpydc. (b) $N_2$ adsorption-desorption isotherms of **Ce-MOF** and **Ce-MOF-Ru$^{II}$-bpy**. (c) Pore size distribution of **Ce-MOF** and **Ce-MOF-Ru$^{II}$-bpy**. (d) UV-vis spectra of **Ce-MOF** and **Ce-MOF-Ru$^{II}$-bpy**. (e) Tauc plot of **Ce-MOF** and **Ce-MOF-Ru$^{II}$-bpy** for evaluating the optical bandgap. (f) High-resolution TEM images of **Ce-MOF-Ru$^{II}$-bpy**. (g) FESEM images of **Ce-MOF-Ru$^{II}$-bpy**. (h) XPS spectrum of Ce 3d in **Ce-MOF-Ru$^{II}$-bpy**. (i) XPS spectra of Ru 3d and C 1s in **Ce-MOF-Ru$^{II}$-bpy**. (j) XPS spectra of Ru 3p in **Ce-MOF-Ru$^{II}$-bpy**. (k) XPS spectra of N 1s in **Ce-MOF-Ru$^{II}$-bpy**. (l) XPS spectra of O 1s in **Ce-MOF-Ru$^{II}$-bpy**.

$[Ce_6O_5(OH)_3(bpydc)_5(H_2O)_2]$. Next, $N_2$ adsorption measurement was performed at 77 K to evaluate the porosity of **Ce-MOF**, which exhibited a predominant type-I adsorption profile (Fig. 1b, Fig. S7). Notably, a small hysteresis was found in the high-pressure region ($P/P_0$ = 0.6-1), and the $N_2$ uptake was found to be 630 $cm^3\ g^{-1}$ with Brunauer–Emmett–Teller (BET) surface area of 2024 $m^2\ g^{-1}$ (Fig. 1b). The corresponding pore size distribution by the NLDFT method suggested the presence of additional mesopores distributed between 2.5 to 10 nm with the peak maxima at 3.2 and 4.8 nm and micropore at 1.4 nm (Fig. 1c).[9] The presence of dual-porosity further corroborates the structural defect due to the missing linker in the pristine **Ce-MOF**. **Ce-MOF** possessed an intense absorption in the UV region at wavelengths 281 and 325 nm due to π→π* and n→π* transition of bpydc linker, respectively (Fig. 1d and 1e).[22] Consequently, the lack of visible light absorption ability disbarred the pristine **Ce-MOF** use as a photocatalyst for $CO_2$ reduction.

Therefore, to mitigate this limitation, pristine **Ce-MOF** was post-synthetically modified with $[Ru(bpy)_2]^{2+}$, which is an excellent photosensitizer (PS) in the field of photocatalysis due to strong visible light absorption, long excited-state lifetime, and acts as an outstanding electron donor to the catalytic centre.[23] The N,N′ chelating site of $bpydc^{2-}$ linker facilitated the coordination of the $[Ru(bpy)_2]^{2+}$ to form $[Ru(bpydc)(bpy)_2]^{2+}$ (PS) into a perfectly matched MOF pore (Fig. S8,S9). PXRD studies indicated that **Ce-MOF-Ru$^{II}$-bpy** prepared at ambient condition and under daylight exhibited a similar diffraction pattern as of **Ce-MOF** (Fig. 1a). FESEM and TEM images showed cubic morphology and particle sizes remained intact after post-synthetic modification. (Fig. 1f,1g). EDX and elemental mapping showed that the Ce, Ru, O, C, N were evenly distributed in **Ce-MOF-Ru$^{II}$-bpy** (Fig. S10, Table S1).

Inductively coupled plasma-optical emission spectrometry (ICP-OES) analysis of digested **Ce-MOF-Ru$^{II}$-bpy** showed a Ce:Ru ratio of 6:1.84. The elemental composition and oxidation state of the **Ce-MOF-Ru$^{II}$-bpy** was investigated using X-ray photoelectron spectroscopy (XPS) analysis (Fig. 1h-1l and S11). The XPS spectra of pristine **Ce-MOF** demonstrated the presence of a mixed valence state of Ce$^{III/IV}$ (Fig. S12b). The peaks at a binding energy value of 916, 908.1, 902.8, 897.6, 888.02, and 881.83 eV corresponded to Ce$^{IV}$, whereas the peaks at 905.69, 899.86, 884.67, and 880.44 eV attributed to Ce$^{III}$.[24, 25] The ratio of Ce$^{III}$ and Ce$^{IV}$ was calculated by fitting with a Gaussian distribution which indicated 94.77 % of cerium present in Ce$^{IV}$ state. Interestingly, in **Ce-MOF-Ru$^{II}$-bpy** the abundance of Ce$^{III}$ increased to 47.41% due to the feasibility of highly favourable electron transfer from PS to the low lying 4f orbital of Ce$^{IV}$ at day light condition (Fig. 1h).[9, 10, 13-16] The formation of the Ru$^{III}$ in **Ce-MOF-Ru$^{II}$-bpy** was also confirmed by the XPS analysis (Fig. 1i and 1j). The Ru 3d spectra were deconvoluted into two doublets ($3d_{5/2}$ and $3d_{3/2}$) at 281.19 and 286.0 eV as well as 282 and 286.47 eV attributed to the Ru$^{II}$ and Ru$^{III}$ species, respectively.[26] The C 1s spectra overlapped with Ru 3d spectra and fitted into six Gaussian lines at around 284.9, 285.7, 287.3, 288.15, 288.98, 291.05 eV, assigned to the C1s core signal of C-C, C-H, C-O, O-C=O, C-N, C=O, respectively (Fig. 1i). In addition, Ru 3p showed two doublets ($3p_{3/2}$ and $3p_{1/2}$) at 461.4 and 483.72 eV as well as 463.46 and 486.63 eV, which corresponds to Ru$^{II}$ and Ru$^{III}$ species, respectively (Fig. 1j).[27] Hence, XPS studies revealed the coexistence of both the species, Ru$^{II}$ and Ru$^{III}$, in **Ce-MOF-Ru$^{II}$-bpy**. Moreover, the successful coordination of $[Ru(bpy)_2]^{2+}$ with N,N′-chelating centre of bpydc linker was also confirmed by N 1s XPS analysis (Fig. 1k). Pristine **Ce-MOF** comprised of only one peak at 398.2 eV corresponds to N 1s (Fig. S12c).[28] However, after coordination of Ru to the N, N′-chelating centre of bpydc the N 1s spectra showed a broad asymmetric peak and deconvoluted into two peaks, 397.8 and 400 eV corresponding to uncoordinated pyridinic N and Ru-N quaternary N species, respectively (Fig. 1k).[28, 29] This result further signifies the presence of two types of N in **Ce-MOF-Ru$^{II}$-bpy**, hence confirming the successful coordination of $[Ru(bpy)_2]^{2+}$ in **Ce-MOF**. Moreover, O 1s spectra were deconvoluted into three peaks at 528, 530.62, 532.9 eV, attributed to Ce-O-Ce, Ce-O-C, and COOH bonds (Fig. 1l).[30, 31] Further, X-ray structure absorption near edge (XANES) was performed to confirm the average oxidation state of **Ce-MOF** and **Ce-MOF-Ru$^{II}$-bpy** (Fig. 2a, 2b, and Fig. S13). This analysis is very reliable for assessing the oxidation state of Ce, since XANES features of Ce-$L_3$ are known to be largely dependent on the average oxidation state of Ce atom and much less affected by the discrepancy in the local geometry.[32] At the Ce-$L_3$ edge, upon transition from Ce$^{IV}$ to Ce$^{III}$, the shape of the spectrum changes drastically.[32] The peak at 5729.5 eV and 5739.09 eV corresponds to Ce$^{IV}$ oxidation state while 5726.38 eV corresponds to Ce$^{III}$ oxidation state (Fig. 2a).[33, 34] To extract Ce$^{III}$ concentration from XANES data of pristine **Ce-MOF** and **Ce-MOF-Ru$^{II}$-bpy**, the spectra were curve-fitted with an arctangent function to simulate the edge jump and Gaussian functions for peak features.[33, 35, 36] The concentrations of Ce$^{III}$ and Ce$^{IV}$ in pristine **Ce-MOF** are about 6% and 94%, respectively, as shown in fig. S13. After incorporating $[Ru(bpy)_2Cl_2]$, the % of Ce$^{III}$ increased up to 49.27% in **Ce-MOF-Ru$^{II}$-bpy** (Fig. 2b). These findings corroborated well with the XPS results. Furthermore, the Ru K-edge XANES spectra in **Ce-MOF-Ru$^{II}$-bpy** showed the edge between Ru$^{II}$ and Ru$^{III}$, implying that Ru exists in both 2+ and 3+ valance states, which is compatible with the XPS results (Fig. S14). To support the aforementioned statement of the redox state of Ce over **Ce-MOF** and **Ce-MOF-Ru$^{II}$-bpy**, electron paramagnetic resonance (EPR) studies were carried out (Fig. S15). The **Ce-MOF** showed no significant EPR signal under daylight. (Fig. S15). Importantly, after incorporating $[Ru(bpy)_2]^{2+}$ into the **Ce-MOF**, **Ce-MOF-Ru$^{II}$-bpy** exhibited broad and strong EPR spectra at g = 1.976, and g = 2.14, corresponding to Ce$^{III}$ and Ru$^{III}$, respectively.[37, 38] This result indicated a facile electron transfer from the $[Ru(bpy)_2]^{2+}$ to the Ce$^{IV}$ at ambient day light condition. With further visible light irradiation, Ce$^{III}$ and Ru$^{III}$ peaks intensity increased due to further electron transfer (Fig. S15). To understand the coordination environment of the Ru in **Ce-MOF-Ru$^{II}$-bpy**, an extended X-ray absorption fine structure (EXAFS) measurement was performed. As shown in Fig. S16 **Ce-MOF-Ru$^{II}$-bpy** exhibited a similar Ru K-edge EXAFS magnitude to that of its corresponding molecular model $[Ru(bpy)_3]Cl_2$ and showed only Ru-N scattering. Quantitative EXAFS curve-fitting analyses for **Ce-MOF-Ru$^{II}$-bpy** verify the coordination number of Ru and bond distance of Ru-N and found to be 6 and 2.07 Å, respectively (Fig. 2c, S17 and Table S2).[39] Additionally, in Fig. 2d, the wavelet transform contour plots of **Ce-MOF-Ru$^{II}$-bpy** showed only one intensity maximum at 5.9 Å$^{-1}$, corresponding to Ru-N coordination. Moreover, no intensity maximum related to Ru-Ru contribution (10.05 Å$^{-1}$) can be detected at high coordination shells when compared with the WT plot of Ru foil in Fig. 2d.

Next, $N_2$ adsorption measurement at 77 K illustrated that the introduction of $[Ru(bpy)_2Cl_2]$ into the framework leads to a decrease in the uptake (~ 272 cm$^3$ g$^{-1}$) with the corresponding surface area of 873 m$^2$ g$^{-1}$ (Fig. 1b). Importantly, the small hysteresis present in the pristine **Ce-MOF** disappeared in **Ce-MOF-Ru$^{II}$-bpy**. The pore size distribution showed a reduction of pore size from 1.4 nm to 0.8 nm in the micropore and complete depletion of the mesopore (Fig. 1c). The UV-vis spectra of **Ce-MOF-Ru$^{II}$-bpy** compared with the as-synthesized **Ce-MOF** showed an absorption edge extending about 550 nm with absorption maxima at 445 nm and 492 nm (Fig. 1d). Importantly, the bands at 445 nm and 492 nm corresponded to $^1$MLCT and $^3$MLCT ($Ru^{II}_{d\pi} \rightarrow \pi^*_{bpy}$) transitions of $[Ru(bpydc)(bpy)_2]^{2+}$ respectively, further demonstrating the immobilization of $[Ru(bpy)_2]^{2+}$ into the MOF pore.[40] To confirm this, $[Ru(bpy)_3]^{2+}$ ligand was also prepared, which showed a similar MLCT transition with absorption maxima at~ 450 nm in $CH_3CN$ (Fig. S18). Furthermore, to get insight into the redox behaviour of **Ce-MOF-Ru$^{II}$-bpy,** cyclic voltammetry (CV) experiment was carried out (Fig. S19). A reversible redox peak at $E^1_{1/2} = 1.45$ V vs. Ag/AgCl was attributed to the Ce$^{III}$/Ce$^{IV}$

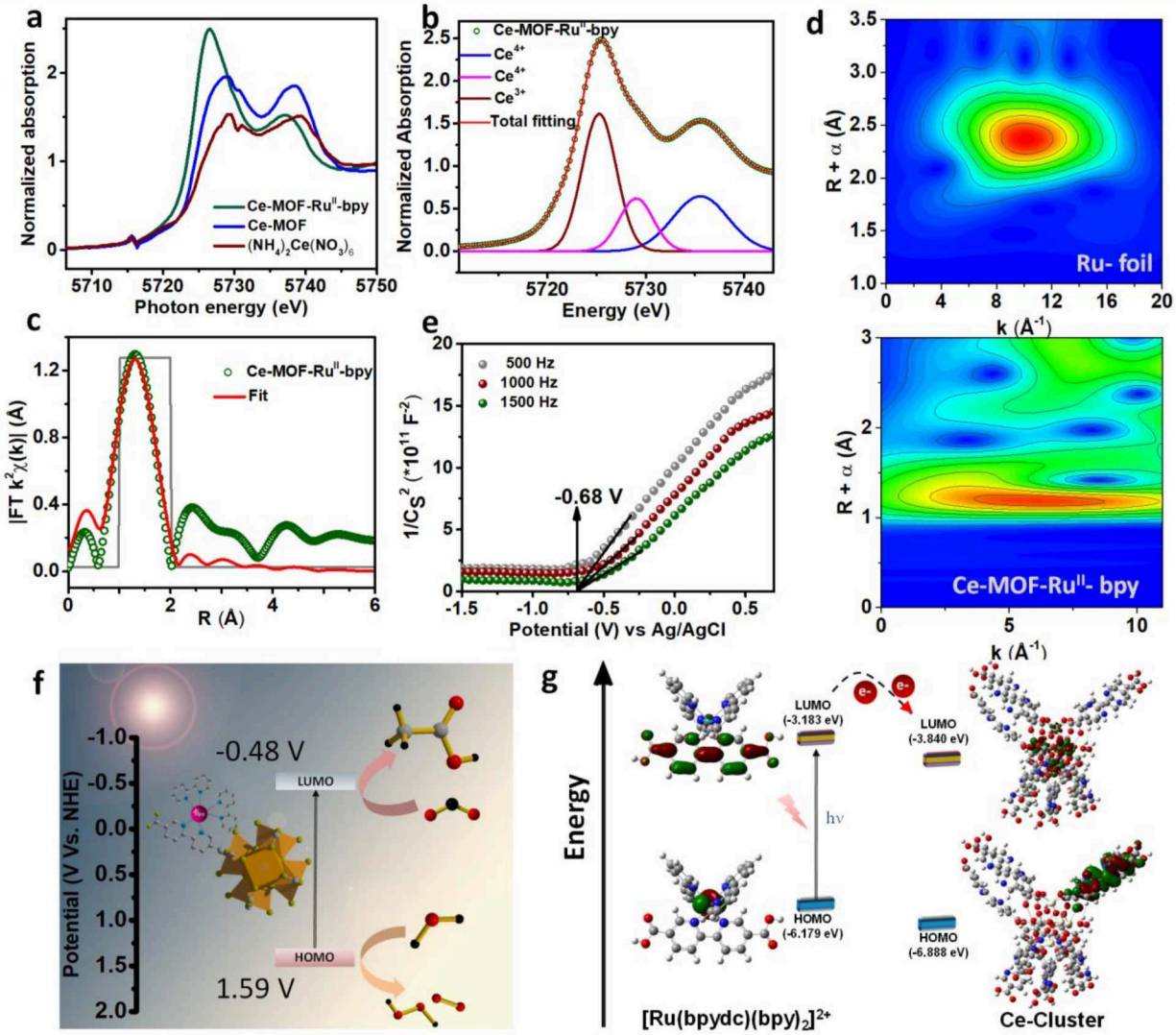


**Fig. 2** (a) Experimental Ce L3-edge XANES spectra of **Ce-MOF-Ru$^{II}$-bpy**, **Ce-MOF** and $(NH_4)_2Ce(NO_3)_6$. (b) Ce L3-edge XANES spectrum and fitting peaks of **Ce-MOF-Ru$^{II}$-bpy**. (c) Experimental and fitted EXAFS data in R space of $[Ru(bpydc)(bpy)_2]Cl_2$ in **Ce-MOF-Ru$^{II}$-bpy**. (d) Wavelet transform for the k3-weighted EXAFS signal of Ru foil and $[Ru(bpydc)(bpy)_2]Cl_2$ in **Ce-MOF-Ru$^{II}$-bpy**. (e) Mott–Schottky plot for **Ce-MOF-Ru$^{II}$-bpy** in 0.2 M $Na_2SO_4$ aqueous solution. (f) Energy diagram of the HOMO and LUMO levels of **Ce-MOF-Ru$^{II}$-bpy**. (g) HOMO–LUMO positioning of the Ru-photosensitizer $[Ru(bpydc)(bpy)_2]Cl_2$ and Ce-Cluster, showing the possibility of charge transfer.

redox pair (Fig. 19a).[41] Apart from this, a reversible redox peak was also observed at $E^1_{1/2} = 1.19$ V vs Ag/AgCl corresponding to $Ru^{II}/Ru^{III}$ redox pair (Fig. 19b).[42]. Moreover, time-dependent density functional theory (TDDFT) calculations were performed to assess the experimentally obtained MLCT bands in the absorption spectrum. TDDFT calculations showed similar theoretical absorption bands at 457.87 nm and 498.64 nm which can be attributed to HOMO-2 to LUMO and HOMO-1 to LUMO transitions, respectively (Fig. 1f, Fig. S20 and Table S3). Ultimately, the molecular orbital analysis revealed those transitions as $^1$MLCT and $^3$MLCT transitions, respectively which attributed the experimental absorption bands at 445 nm and 492 nm, respectively (Fig. 1f, Fig. S20 and Table S3).

**Thermodynamic feasibility for the $CO_2$ reduction reaction**

Next, the Mott-Schottky measurement of **Ce-MOF-Ru$^{II}$-bpy** was performed at a frequency of 500, 1000 and 1500 Hz to elucidate the thermodynamic feasibility of $CO_2$ reduction. As shown in Fig. 2e, the positive slope value of $C^{-2}$ indicated the n-type semiconducting nature of the catalyst. The flat band value was calculated from the intercept of the axis with a potential value of -0.68 V vs Ag/AgCl (-0.48 V w.r.t NHE at pH 7).

Generally, for n-type semiconductors, the conduction band (LUMO) can be determined to be almost equal to the flat band potential. Based on the Tauc plot, the optical bandgap was calculated to be 2.07 eV for **Ce-MOF-Ru$^{II}$-bpy** (Fig. 1g). Accordingly, the valence band was estimated to be 1.59 V, which is more positive than the oxidation potential of $H_2O/O_2$, indicating the ability of **Ce-MOF-Ru$^{II}$-bpy** to reduce $CO_2$ in water (Fig. 2f). Moreover, DFT calculation revealed that the lowest unoccupied molecular orbital (LUMO) of Ce-oxo cluster is located on cerium which is hugely advantageous compared to other UiO-66 architecture with different metals (M) ions (M = Zr, Hf, Th, Ti, U).[9] Molecular orbital (MO) analysis further showed that the LUMO of Ce-oxo cluster is low lying compared to the LUMO of $[Ru(bpydc)(bpy)_2]^{2+}$, which suggested facile electron transfer from the LUMO of PS to the LUMO of Ce-oxo cluster (Fig. 2g). Moreover, $CO_2$ adsorption measurements at 298 K were carried out for pristine **Ce-MOF** and post-modified **Ce-MOF-Ru$^{II}$-bpy**, which showed uptake of 37 $cm^3\ g^{-1}$ and 19 $cm^3\ g^{-1}$, respectively at saturation (Fig. S21). This result indicated the porous feature of **Ce-MOF-Ru$^{II}$-bpy** would help $CO_2$ molecules to interact with the catalytic site during photocatalytic reaction.

**Photocatalytic $CO_2$ reduction reaction**

To assess the catalytic performance, photocatalytic reduction of $CO_2$ over **Ce-MOF-Ru$^{II}$-bpy** was performed in pure water under visible light irradiation. The photo reduced liquid products were analyzed and quantified by $^1$H NMR spectroscopy, whereas gas chromatography-mass spectrometry (GC-MS) was used to quantify gaseous products. It was found that the major product under the photocatalytic process was $CH_3COOH$ under visible light irradiation (Fig. 3a,3b, Fig. S22-S24). As shown in Fig. 3a, the production of $CH_3COOH$ was continuously increased with irradiation time, and a total yield of 1133 µmol $g^{-1}$ was obtained after 10 h of irradiation. The corresponding maximum production rate for $CH_3COOH$ production was found to be 128 µmol $g^{-1}$ $h^{-1}$. Apart from acetic acid production, a very small amount of $H_2$ (65 µmol $g^{-1}$) was also generated in the reaction system. No other product was obtained from $CO_2$ photoreduction, indicating an extremely high selectivity (99.5%) for acetum production. The apparent quantum efficiency for $CH_3COOH$ production was calculated to be 0.93% in water, which is significantly higher than most of the reports till date (Fig. S25). [3, 43] Next, a series of control experiments were conducted to understand the role of $[Ru(bpy)_3]^{2+}$ moiety and Ce-cluster into the MOF framework

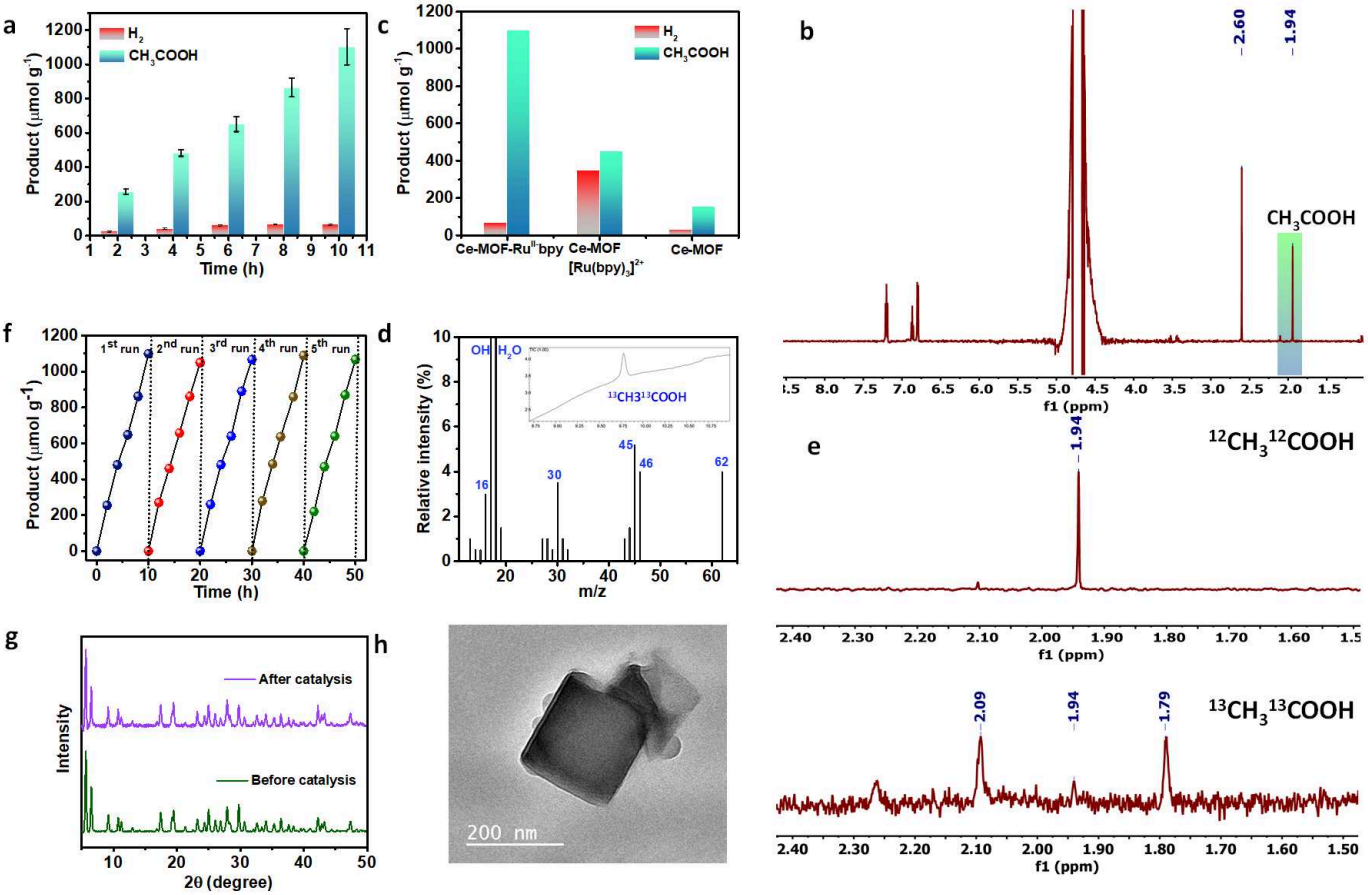


**Fig. 3** Photocatalytic $CO_2$RR performance. (a) acetic acid production as a function of irradiation time over **Ce-MOF-Ru$^{II}$-bpy** as catalyst in pure water medium. (b) Comparison of acetic acid production of **Ce-MOF-Ru$^{II}$-bpy** and **Ce-MOF** in pure water medium under visible light irradiation. (c) $^1$H NMR spectra of the obtained acetic acid product in $CO_2$-saturated water solution. (d) Mass spectra extracted from GC-MS analysis of acetic acid product from $^{13}CO_2$ reduction over **Ce-MOF-Ru$^{II}$-bpy** in water. (e) $^1$H NMR spectra of the obtained acetum product in $CO_2$-saturated water solution by using different $^{12}CO_2$ and $^{13}CO_2$ gas over **Ce-MOF-Ru$^{II}$-bpy** catalyst. (f) Recyclability study for the photoreduction of $CO_2$ (where 5 mg sample was used for this measurement) in water medium. (g) Comparison of PXRD patterns of the as-prepared **Ce-MOF-Ru$^{II}$-bpy** before and after performing catalysis under similar experimental condition. (h) TEM images of **Ce-MOF-Ru$^{II}$-bpy** after catalysis under similar experimental condition.

(Fig. 3c, S26). The catalytic activity of pristine **Ce-MOF** is less efficient (produced 152.5 µmol $g^{-1}$ of $CH_3COOH$ along with 32 µmol $g^{-1}$ of $H_2$) which can be attributed to the poor visible light absorption by the **Ce-MOF** (Fig. 3c). However, $[Ru(bpy)_3]Cl_2$ produced 285 µmol $g^{-1}$ of $H_2$ along with a trace amount of CO and $CH_4$ in water medium (Fig. S26, Table S4). A physical mixture of **Ce-MOF** along with $[Ru(bpy)_3]Cl_2$ produced 450 µmol $g^{-1}$ of $CH_3COOH$ along with 350 µmol $g^{-1}$ of $H_2$ (Fig. 3c and Table S4). No $CH_3COOH$ was detected when the reaction was carried out in the absence of a catalyst or in the Ar atmosphere, or in dark conditions indicating the product was originated from the photocatalytic reduction of dissolved $CO_2$ (Fig. S26 and Table S4). To further confirm the origin of $CH_3COOH$, the isotopic experiment was carried out with $^{13}CO_2$ (Fig. 3d, 3e and S27). The liquid products were collected after 6 h irradiation and identified with GC-MS and NMR. In the mass spectrum, the molecular ion peak at m/z =62, can be ascribed to $^{13}CH_3{}^{13}COOH$ (Fig. 3d, and S27). Furthermore, a peak at m/z = 43 corresponds to the fragmentation of $CH_3CO^+$ during the reaction with $^{12}CO_2$, shifted to m/z = 45 upon replacement with $^{13}CO_2$ (Fig. 3d, and S27). This trend was also reflected in the fragments $CH_3$ and COOH, which showed their corresponding isotopic mass fragments at 16 and 46 instead of 15 and 45. This data was further validated by performing $^1H$ NMR spectroscopy. As shown in Fig. 3e, if $^{12}CO_2$ gas was used for photoreduction, a singlet peak at 1.94 ppm appeared, which is the characteristic proton peak of the methyl group in $CH_3COOH$.[2, 23] Of note, if the carbon source was changed to $^{13}CO_2$, the methyl proton split into two peaks at 1.94 due to coupling between $^1H$ and $^{13}C$ with a coupling constant of 120 Hz (Fig. 3e). These results strongly confirm that the produced $CH_3COOH$ indeed originated from the dissolved $CO_2$ rather than any organic compound decomposition. Most importantly, to evaluate the catalyst stability under the photocatalytic condition, the used sample was recovered from the reaction media by centrifugation, washed, and vacuum dried for the recycling test (Fig. 3f). The results of cycling performance demonstrated the photocatalytic activity of **Ce-MOF-$Ru^{II}$-bpy** for $CH_3COOH$ production was well maintained even after five consecutive cycles for a total of 50 h. The PXRD pattern of the recovered sample after catalysis exhibited no changes indicating the retention of structural integrity (Fig. 3g). The TEM images of the recovered sample also showed the same morphology as freshly prepared **Ce-MOF-$Ru^{II}$-bpy** (Fig. 3h). Moreover, post-catalytic UV-vis and FT-IR analysis exhibited similar characteristics as freshly prepared **Ce-MOF-$Ru^{II}$-bpy** (Fig. S28,S29). During the course of photoirradiation, oxygen was found as a major oxidative product, and a total amount of 1946 µmol $g^{-1}$ of $O_2$ was produced in 10 h (Fig. S30). During this process, 98.4 µmol $g^{-1}$ of $H_2O_2$ was also detected as analyzed by the $FeCl_2$/KSCN and UV-vis spectrophotometric method.[44, 45] These results indicated that $H_2O$ provides the protons for acetic acid generation (Fig. S31).

**Insight into the $CO_2$ reduction mechanism and exploration of the charge transfer pathway**

Next, photo/electrochemical measurements were performed to understand the improved catalytic performance of **Ce-MOF-$Ru^{II}$-bpy** compared to pristine **Ce-MOF**. First, the emission properties of **Ce-MOF-$Ru^{II}$-bpy** and **Ce-MOF** was studied to understand the confinement effect of MOF pore and excited state electron transfer from the PS to catalytic center (Ce-oxo cluster). The photoluminescence spectra of **Ce-MOF** exhibited bands at 462 nm and 566 nm ($\lambda_{ex}$ = 350 nm) (Fig. S32). The photoluminescence spectra of bpydc linker showed a band at 464 nm ($\lambda_{ex}$ = 350 nm) (Fig. S33). These two emission bands of the **Ce-MOF** are attributed to the ligand to ligand charge transfer transition (LLCT, 462 nm) and ligand to metal charge transfer transition (LMCT, 566 nm), respectively. After the encapsulation of $[Ru(bpy)_2]^{2+}$ inside the **Ce-MOF** pore, **Ce-MOF-$Ru^{II}$-bpy** showed a broad emission peak at 650 nm corresponding to $^3$MLCT transition of $[Ru(bpydc)(bpy)_2]^{2+}$ moiety when excited at 470 nm (Fig. 4a).[40] The time-resolved photoluminescence spectra of **Ce-MOF-$Ru^{II}$-bpy** showed an average lifetime of 42 ns, which is significantly smaller as compared to free $[Ru(bpy)_3]Cl_2$ complex (185.5 ns) in solid-state (Fig. 4b).[46] These results clearly indicate that the $^3$MLCT excited-state of $Ru^{II}$ is immediately quenched by fast electron transfer to the $Ce^{IV}$- oxo cluster. Electron transfer from the PS to the M-oxo cluster (M = metal) is highly feasible in the case of $Ce^{IV}$ as compared to other metal ions ($M^{IV}$ = Zr, Hf, Th and Ti) having UiO-66 framework due to the close value of energy levels between PS and $Ce^{IV}$- oxo cluster, which helps facile electron transfer (Fig. 2g). Next, the transient photocurrent experiment was performed (Fig. S34). The photocurrent response of the **Ce-MOF-$Ru^{II}$-bpy** sample was 11.65 µA $cm^{-2}$, corresponding to an enhancement of 31.09 % compared to the pristine **Ce-MOF**, which points to better photocatalytic activity of **Ce-MOF-$Ru^{II}$-bpy**due to large photo-induced charge migration. Moreover, **Ce-MOF-$Ru^{II}$-bpy** exhibited a smaller semi-circle (2 fold decrease) than pristine **Ce-MOF** in the electrochemical impedance spectra, reflecting the lower charge transfer resistance in **Ce-MOF-$Ru^{II}$-bpy** (Fig. S35). The charge transfer from the PS to the $Ce^{IV}$ was further confirmed by *in-situ* UV-vis spectroscopy using a spectro-electrochemical set-up with visible light irradiation, conducted on the dispersion state in water (Fig. 4c). The absorption spectrum of **Ce-MOF-$Ru^{II}$-bpy** was recorded with light irradiation, and a

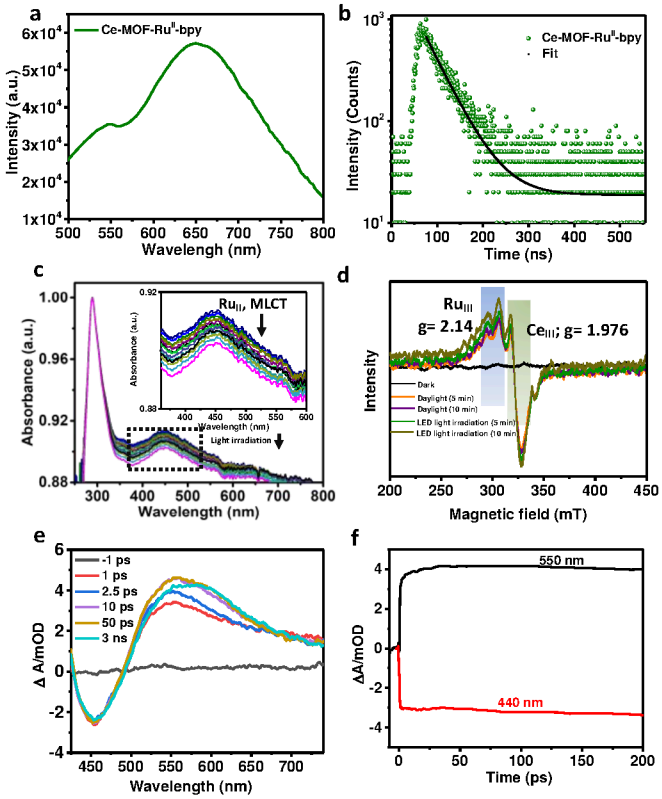


**Fig. 4** Different spectroscopic characterization of **Ce-MOF-Ru$^{II}$-bpy**. (a) Photoluminescence spectra **of Ce-MOF-Ru$^{II}$-bpy**. ($\lambda_{ex}$ = 460 nm) (b) Time-resolved photoluminescence (TRPL) decay of **Ce-MOF-Ru$^{II}$-bpy**. (c). Time-dependent light irradiated UV-vis spectra of **Ce-MOF-Ru$^{II}$-bpy.** (d) EPR spectra of **Ce-MOF-Ru$^{II}$-bpy_d** under dark conditions, exposed under visible light and irradiated with a LED visible light source (λ=380-780 nm). (e) Transient absorption spectra of **Ce-MOF-Ru$^{II}$-bpy** at different time delays. (f) Decay kinetics of transient spectra at 455 and 550 nm for **Ce-MOF-Ru$^{II}$-bpy**.

spectral change was monitored with post and pre-light irradiation. Fig. 4c clearly showed with light irradiation, the intensity of MLCT band ($Ru^{II}$ $d\pi \rightarrow \pi^*_{bpy}$) at 450 nm gradually decreased. These spectral changes indicated enhanced electron transfer from the $Ru^{II}$ to the Ce-oxo cluster with light irradiation. To understand that the daylight acts as a stimulus for the electron transfer from PS species to $Ce^{IV}$ in **Ce-MOF-Ru$^{II}$-bpy**, we have incorporated $[Ru(bpy)_2]^{2+}$ in **Ce-MOF** under completely dark condition, and the resulting MOF denoted as **Ce-MOF-Ru$^{II}$-bpy_d**. The XPS spectra of **Ce-MOF-Ru$^{II}$-bpy_d** suggested the presence of negligible amount of $Ce^{III}$ (9.84 %) similar to as-synthesized pristine **Ce-MOF**. Also the absence of $Ru^{III}$ species in that sample clearly ruled out the electron transfer from PS to the $Ce^{IV}$ in the dark state (Fig. S36, S37). Additionally, we have performed the EPR study of the same sample under dark condition. Notably, the absence of any recognizable EPR signal in **Ce-MOF-Ru$^{II}$-bpy_d** demonstrated the daylight acts as a stimulus for the significant charge-separation in **Ce-MOF-Ru$^{II}$-bpy** prepared under daylight condition (Fig. 4d). The electron transfer from the PS to the catalytic site of the MOF was further investigated using transient absorption (TA) spectroscopy (Fig. 4e and 4f). Upon photoexcitation with 400 nm laser pulse, TA spectra of **Ce-MOF-Ru$^{II}$-bpy** showed a strong negative signal at ~455 nm due to depletion of the ground state population of PS (Fig. 4e). A broad excited state absorption (ESA) band spanning over 520-750 nm was seen to grow in the early time scale and almost remained unchanged up to the available optical delay window of the TA setup (2 ns). To understand the origin of the ESA band in **Ce-MOF-Ru$^{II}$-bpy**, TA experiments were performed with $[Ru(bpy)_2Cl_2]$ solution (Fig. S38). Like **Ce-MOF-Ru$^{II}$-bpy**, TA spectra of $[Ru(bpy)_2Cl_2]$ also showed a ground state bleach (GSB) signal at ~475 nm. The red shift in the GSB band in $[Ru(bpy)_2Cl_2]$ as compared to **Ce-MOF-Ru$^{II}$-bpy** (455nm) is in accordance with their absorption spectra (Fig. S18). However, unlike **Ce-MOF-Ru$^{II}$-bpy**, the TA spectra of $[Ru(bpy)_2Cl_2]$ does not show any ESA band in the spectral region of 550 nm. Instead, a weak and broad ESA band is observed at > 600 nm due to the $^3$MLCT state of Ru(II) complex.[47] Thus, the appearance of the 550 nm ESA band in **Ce-MOF-Ru$^{II}$-bpy** is clearly due to the incorporation of $[Ru(bpy)_2Cl_2]$ in the **Ce-MOF**. A similar ESA band was reported for a Ru(II)-polypyridylcomplex anchored on $TiO_2$ nanoparticles. It was shown that the ejection of an electron from the Ru complex to $TiO_2$ nanoparticles results in the formation of ESA band at ~550 nm, which was characterized as the $Ru^{III}$ complex.[48] Hence, the ESA band at 550 nm observed in our study can be assigned to the $Ru^{III}$ complex. Thus, the formation of $Ru^{III}$ complex in **Ce-MOF-Ru$^{II}$-bpy** upon photoexcitation clearly indicates the transfer of electron from the photoexcited PS to the $Ce^{IV}$ catalytic centre. The kinetics of the GSB and the ESA bands at 455 nm and 550 nm, respectively are shown in Fig. 4f. The GSB band remains constant even upto 2 ns suggesting extremely long recovery time for the ground state of PS. However, the kinetic analysis of the ESA band at 550 nm showed a growth component (2.7 ps) followed by a very long decay component (>2 ns). Since, the intersystem crossing (ISC) in $[Ru(bpy)_2Cl_2]^{2+}$ complex is reported to be very fast (~30-100 fs), the relatively slow growth of the $Ru^{III}$ complex clearly indicates that the electron transfer takes place from the $^3$MLCT state of PS.[47, 49] Further, extremely slow recovery of the GSB signal clearly indicates that the charge recombination process for PS system embedded in **Ce-MOF** matrix is extremely slow. The slow charge recombination process indicates that the photo-excited electron from the PS is available for a reasonably long time. Such efficient electron transfer and extremely slow recombination process support the higher catalytic activity of PS system embedded in **Ce-MOF** system.

To further understand the reaction intermediate during the reduction process of $CO_2$ molecule, *in situ* DRIFT measurements were performed (Fig. 5a, and S39). All FTIR spectra were recorded by subtracting the spectra of **Ce-MOF-Ru$^{II}$-bpy** without $CO_2$, $H_2O$ vapour and light under vacuum. After the introduction of the $CO_2$, a peak at 2343 $cm^{-1}$ was observed, corresponding to adsorbed $CO_2$.[2] After photo irradiation of the **Ce-MOF-Ru$^{II}$-bpy** sample for 10 min, several new peaks appeared. The peaks at 1400 and 1675 $cm^{-1}$ could be accredited to the symmetric and asymmetric stretching of $HCO_3$*, respectively.[1, 36, 50, 51] Moreover, the peaks at 1249 $cm^{-1}$ correspondto $CO_2^-$*.[52, 53] The peak intensity of surface

ARTICLE

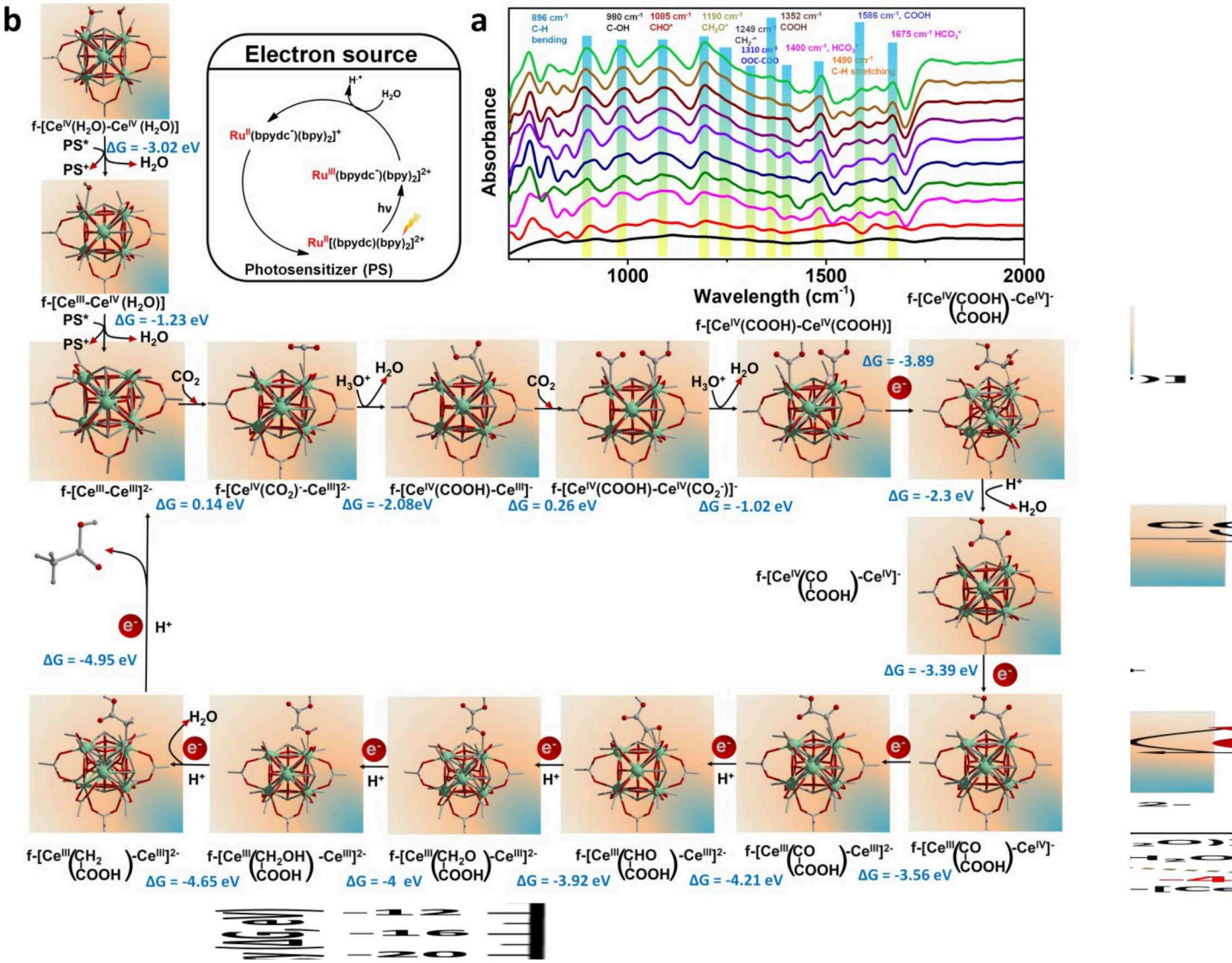


**Fig. 5** Understanding the reaction mechanism for the photoreduction of $CO_2$ to $CH_3COOH$. (a) Time-dependent in situ diffuse reflectance FT-IR spectra for $CO_2$ reduction in a mixture of $CO_2$ and $H_2O$ vapour on **Ce-MOF-Ru$^{II}$-bpy** in the dark (background) and under visible light irradiation (LED lamp, I =420 nm). Irradiation time 20, 40, 60, 80, 100, 120, 140, 160 and 180 min, respectively. (b) Schematic illustration of the proposed reaction mechanism for the $CO_2$-to-$CH_3COOH$ photo-conversion on the **Ce-MOF-Ru$^{II}$-bpy** system in aqueous solvent (f = fragment).

adsorbed $CO_2$ ($CO_2^{-}$*) decreased with irradiation. The peak at 1310 $cm^{-1}$ belongs to OOC-COO.[54] The peak intensity of OOC-COO increased during 1$^{st}$ 40 min then decreased during the course of the light irradiation, indicating OOC-COO is a crucial intermediate for acetate formation over **Ce-MOF-Ru$^{II}$-bpy**. The peak that appeared at 1085 $cm^{-1}$ was assigned to the characteristic band for CHO* formation.[36] The peak at 1190 $cm^{-1}$ corresponds to the CO stretching frequency of $CH_2O$*.[55] The bands at 1352 $cm^{-1}$ and 1586 $cm^{-1}$ suggested the formation of COOH.[3, 54] The band that appeared at 980 $cm^{-1}$ correspond to the C-O stretching band and belongs to the newly formed C-OH group.[3] In addition, the bands at 1490 $cm^{-1}$

and 896 $cm^{-1}$ are related to the C-H bending vibration and the band at 2900 $cm^{-1}$ was assigned to C-H stretching vibration.[56] Moreover, density functional theory (DFT) calculations were performed to gain insight into the mechanism involved in the photocatalytic $CO_2$RR. Based on earlier literature reports, *in situ* DRIFTS study and DFT calculation, a possible catalytic cycle for the photocatalytic $CO_2$RR on **Ce-MOF-Ru$^{II}$-bpy** catalyst has been constructed. Notably, the smallest possible repetitive unit $[Ce_6(\mu_3\text{-}O)_5(\mu_3\text{-}OH)_3(bpydc)_5(H_2O)_2]$ consisting of one Ce-oxo-cluster was considered in DFT calculation, which is represented as **f-[Ce$^{IV}$(H$_2$O)-Ce$^{IV}$(H$_2$O)]** in short for simplicity. The photocatalytic process will be initiated via the photoexcitation of the $[Ru(bpydc)(bpy)_2]^{2+}$ photosensitizer (Fig. 5b, 5c). Upon photoirradiation, the photosensitizer **[Ru$^{II}$(bpydc)(bpy)$_2$]$^{2+}$** will be photoexcited through MLCT to generate **[Ru$^{III}$(bpydc$^{-}$)(bpy)$_2$]$^{2+*}$**, which will then be reductively quenched to afford photo-reduced **[Ru$^{II}$(bpydc$^{-}$)(bpy)$_2$]$^{+}$**. The photo-reduced **[Ru$^{II}$(bpydc$^{-}$)(bpy)$_2$]$^{+}$** will then transfer the photoexcited electron to the low-lying LUMO of Ce-oxo-cluster localized on Ce, which will result in the reduction of the starting catalyst **f-[Ce$^{IV}$(H$_2$O)-Ce$^{IV}$(H$_2$O)]** to afford **f-[Ce$^{IV}$(H$_2$O)-Ce$^{III}$]$^{-}$** with ready removal of $H_2O$ molecule (ΔG = -3.02 eV). In the next step, intermediate **f-[Ce$^{IV}$(H$_2$O)-Ce$^{III}$]$^{-}$** will undergo further photo-reduction and water elimination to produce **f-[Ce$^{III}$-Ce$^{III}$]$^{2-}$** (ΔG = -1.23 eV), which is the active species for the catalytic cycle. Next, **f-[Ce$^{III}$-Ce$^{III}$]$^{2-}$** will undergo oxidative addition of $CO_2$ on a single Ce-centre to afford **f-[Ce$^{IV}$(CO$_2^{-}$)-Ce$^{III}$]$^{2-}$** (ΔG = +0.14 eV) with a very low activation barrier of 0.38 eV, which will lead to the formation of intermediate **f-[Ce$^{IV}$(COOH)-Ce$^{III}$]$^{-}$** (ΔG = -2.08 eV) upon protonation. Intermediate **f-[Ce$^{IV}$(COOH)-Ce$^{III}$]$^{-}$** will then undergo oxidative addition of $CO_2$ on the remaining coordinatively unsaturated proximal Ce-centre also to generate **f-[Ce$^{IV}$(COOH)-Ce$^{IV}$(CO$_2^{-}$)]$^{-}$** (ΔG = +0.26 eV) with a low activation barrier of 0.46 eV, which will get protonated to afford intermediate **f-[Ce$^{IV}$(COOH)-Ce$^{IV}$(COOH)]** (ΔG = -1.02 eV). Next, **f-[Ce$^{IV}$(COOH)-Ce$^{IV}$(COOH)]** will be photo-reduced to generate the crucial C2-bound intermediate **f-[Ce$^{III}$(HOOC-COOH)-Ce$^{IV}$]$^{-}$** (ΔG = -3.89 eV), which was detected in the *in situ* DRIFTS study. The C2-bound intermediate **f-[Ce$^{III}$(HOOC-COOH)-Ce$^{IV}$]$^{-}$** will then afford **f-[Ce$^{IV}$(OC-COOH)-Ce$^{IV}$]** after subsequent protonation and water elimination (ΔG = -2.30 eV). In the next step, intermediate **f-[Ce$^{IV}$(OC-COOH)-Ce$^{IV}$]** will be photo-reduced to **f-[Ce$^{III}$(OC-COOH)-Ce$^{IV}$]$^{-}$** (ΔG = -3.39 eV) which upon further photo-reduction will lead to the formation of **f-[Ce$^{III}$(OC-COOH)-Ce$^{III}$]$^{2-}$** (ΔG = -3.56 eV). In the following steps of the photocatalytic cycle, subsequent proton-coupled reduction of **f-[Ce$^{III}$(OC-COOH)-Ce$^{III}$]$^{2-}$** will lead to the formation of **f-[Ce$^{III}$(OHC-COOH)-Ce$^{III}$]$^{2-}$** (ΔG = -4.21 eV) to **f-[Ce$^{III}$(OH$_2$C-COOH)-Ce$^{III}$]$^{2-}$** (ΔG = -3.92 eV) to **f-[Ce$^{III}$(HOH$_2$C-COOH)-Ce$^{III}$]$^{2-}$** (ΔG = -4.00 eV) which upon further proton-coupled reduction and water elimination will afford **f-[Ce$^{III}$(H$_2$C-COOH)-Ce$^{III}$]$^{2-}$** (ΔG = -4.65 eV). Lastly, intermediate **f-[Ce$^{III}$(H$_2$C-COOH)-Ce$^{III}$]$^{2-}$** will readily produce $CH_3COOH$ upon further proton-coupled reduction (ΔG = -4.95 eV) and the active species **f-[Ce$^{III}$-Ce$^{III}$]$^{2-}$** will be regenerated in the process which will re-enter into the catalytic cycle (Fig. 5b). Thus, *in situ* DRIFT and DFT calculation demonstrated the role of unsaturated proximal Ce$^{IV}$ sites in **Ce-MOF-Ru$^{II}$-bpy** catalyst formed due to the defect of bpydc linker for selective $CO_2$ reduction to acetic acid.

## Conclusion

In summary, we designed an efficient photocatalyst system by grafting $[Ru(bpy)_2Cl_2]$ PS into a stable nanoscale Ce-UiO-66-bpydc-MOF (**Ce-MOF**). **Ce-MOF-Ru$^{II}$-bpy** is highly efficient for visible light-driven $CO_2$ reduction to produce acetic acid with a high production rate of 128 μmol $g^{-1}$ $h^{-1}$. This work is the first experimental report where engrafting of Ru$^{II}$-bipy photosensitizer into a Ce-based MOF (**Ce-UiO-66-bpydc-MOF**) can lead to efficient $CO_2$RR towards C2 product formation with high production yield (1133 μmol $g^{-1}$) and >99 % selectivity. The favourable LMCT from photosensitizer to the low lying 4f orbital of the Ce-oxo cluster and the confinement effect of the MOF nanospace boost the electron transfer efficiency to trigger C-C coupling for selective photoreduction of $CO_2$ in water into C2 product. TDDFT calculation suggested Ce$^{III}$ is the active catalytic site for $CO_2$RR. *In situ* DRIFT and Gibbs free energy calculation unveiled the reaction mechanism for acetic acid production via C-C bond formation. Hence, the introduction of suitable PS, and exploration of pore confinement effect inside the MOF as well as the presence of proximal unsaturated Ce as active catalytic sites with low lying LUMO resulted in selective acetic acid (C2 product) production. We believe this result can lead to a new vista in the field of solar fuel production based on $CO_2$ reduction.

## Author Contributions

S.K. and T.K.M. designed the concept of this work. S.K., and S. Barman performed major experiments. S.K., S. Barman, and T.K.M. analyzed the experimental data and wrote the manuscript. F.A.R. performed the computational study. S. Biswas and T.K.M. collected EXAFS data. S.N.D performed the T.A measurement. All the authors discussed the results and commented on the manuscript.

## Conflicts of interest

The authors declare no conflict of interest.

## Acknowledgements

The authors are grateful for the support and the resources provided by ''PARAM Yukti Facility'' under the National Supercomputing Mission, Government of India at the JNCASR, Bangalore. S.K. and F.A.R. thanks CSIR (Govt. of India) for the fellowship. S.B. thanks JNCASR for the fellowship. TKM acknowledges the Department of Science and Technology (DST, project no.CRG/2019/005951; SPR/2021/000592), RAK-CAM (from UAE), SSL, ICMS, and JNCASR for financial support. SAMat research facility, Sheikh Saqr senior fellowship (TKM), is

 

also gratefully acknowledged. We thank Dr. W. A. Caliebe for assistance in EXAFS measurement at PETRAIII of DESY, Helmholtz Association (HGF), (beamline P64), Germany supported by the DST, government of India. All authors also acknowledge Life Sciences Research, Education and Training at JNCASR (Project No. DBT/JNCASR/D0004/ 2018/00159:- 4547).

## Notes and references

1. J. Zhu, W. Shao, X. Li, X. Jiao, J. Zhu, Y. Sun and Y. Xie, *J. Am. Chem. Soc.*, 2021, **143**, 18233-18241.
2. F. Yu, X. Jing, Y. Wang, M. Sun and C. Duan, *Angew. Chem. Int. Ed.*, 2021, **60**, 24849-24853.
3. S. Sun, M. Watanabe, J. Wu, Q. An and T. Ishihara, *J. Am. Chem. Soc.*, 2018, **140**, 6474-6482.
4. S. Zhu, X. Li, X. Jiao, W. Shao, L. Li, X. Zu, J. Hu, J. Zhu, W. Yan, C. Wang, Y. Sun and Y. Xie, *Nano Lett.*, 2021, **21**, 2324-2331.
5. T. Kunene, L. Xiong and J. Rosenthal, *Proc. Natl. Acad. Sci.*, 2019, **116**, 9693.
6. J. Albero, Y. Peng and H. García, *ACS Catal.*, 2020, **10**, 5734-5749.
7. J.-S. Qin, S. Yuan, L. Zhang, B. Li, D.-Y. Du, N. Huang, W. Guan, H. F. Drake, J. Pang, Y.-Q. Lan, A. Alsalme and H.-C. Zhou, *J. Am. Chem. Soc.*, 2019, **141**, 2054-2060.
8. M. Elcheikh Mahmoud, H. Audi, A. Assoud, T. H. Ghaddar and M. Hmadeh, *J. Am. Chem. Soc.*, 2019, **141**, 7115-7121.
9. X.-P. Wu, L. Gagliardi and D. G. Truhlar, *J. Am. Chem. Soc.*, 2018, **140**, 7904-7912.
10. D. Zhao and C. Cai, *Dyes Pigm.*, 2021, **185**, 108957.
11. S. Sangeetha and G. Krishnamurthy, *Bull. Mater. Sci.*, 2020, **43**, 269.
12. Y. Song, Y. Pi, X. Feng, K. Ni, Z. Xu, J. S. Chen, Z. Li and W. Lin, *J. Am. Chem. Soc.*, 2020, **142**, 6866-6871.
13. Z. Yang, X. Xu, X. Liang, C. Lei, L. Gao, R. Hao, D. Lu and Z. Lei, *Appl. Surf. Sci.*, 2017, **420**, 276-285.
14. Y. Xiong, S. Chen, F. Ye, L. Su, C. Zhang, S. Shen and S. Zhao, *Chem. Commun.*, 2015, **51**, 4635-4638.
15. M. Lammert, M. T. Wharmby, S. Smolders, B. Bueken, A. Lieb, K. A. Lomachenko, D. D. Vos and N. Stock, *Chem. Commun.*, 2015, **51**, 12578-12581.
16. J.-M. Yang, R.-J. Ying, C.-X. Han, Q.-T. Hu, H.-M. Xu, J.-H. Li, Q. Wang and W. Zhang, *Dalton Trans.*, 2018, **47**, 3913-3920.
17. A. Ghosh, S. Karmakar, F. A. Rahimi, R. S. Roy, S. Nath, U. K. Gautam and T. K. Maji, *ACS Appl. Mater. Interfaces*, 2022, **14**, 25220-25231.
18. Z. Hu, Y. Wang and D. Zhao, *Chem. Soc. Rev.*, 2021, **50**, 4629-4683.
19. M. Lammert, C. Glißmann, H. Reinsch and N. Stock, *Cryst. Growth Des.*, 2017, **17**, 1125-1131.
20. Q. Zhang, T. Yang, X. Liu, C. Yue, L. Ao, T. Deng and Y. Zhang, *RSC Adv.*, 2019, **9**, 16357-16365.
21. A. Lin, A. A. Ibrahim, P. Arab, H. M. El-Kaderi and M. S. El-Shall, *ACS Appl. Mater. Interfaces*, 2017, **9**, 17961-17968.
22. S. Bhattacharjee, S. Bera, R. Das, D. Chakraborty, A. Basu, P. Banerjee, S. Ghosh and A. Bhaumik, *ACS Appl. Mater. Interfaces*, 2022, **14**, 20907-20918.
23. S. Karmakar, S. Barman, F. A. Rahimi and T. K. Maji, *Energy Environ. Sci.*, 2021, **14**, 2429-2440.
24. A. Gupta, S. Das, C. J. Neal and S. Seal, *J. Mater. Chem. B*, 2016, **4**, 3195-3202.
25. T. Naganuma and E. Traversa, *Nanoscale*, 2012, **4**, 4950-4953.
26. W. Zhang, M. Kauer, O. Halbherr, K. Epp, P. Guo, M. I. Gonzalez, D. J. Xiao, C. Wiktor, F. X. Liabrés i Xamena, C. Wöll, Y. Wang, M. Muhler and R. A. Fischer, *Chem. Eur. J*, 2016, **22**, 14297-14307.
27. D. J. Morgan, *Surf. Interface Anal.*, 2015, **47**, 1072-1079.
28. S. H. Patil, A. P. Gaikwad, S. D. Sathaye and K. R. Patil, *Electrochim. Acta*, 2018, **265**, 556-568.
29. D. Y. Osadchii, A. I. Olivos-Suarez, A. V. Bavykina and J. Gascon, *Langmuir*, 2017, **33**, 14278-14285.
30. B. Wang, B. Zhu, S. Yun, W. Zhang, C. Xia, M. Afzal, Y. Cai, Y. Liu, Y. Wang and H. Wang, *NPG Asia Mater.*, 2019, **11**, 51.
31. Y. Wang, L. Li, P. Dai, L. Yan, L. Cao, X. Gu and X. Zhao, *J. Mater. Chem. A*, 2017, **5**, 22372-22379.
32. S. Smolders, K. A. Lomachenko, B. Bueken, A. Struyf, A. L. Bugaev, C. Atzori, N. Stock, C. Lamberti, M. B. J. Roeffaers and D. E. De Vos, *ChemPhysChem*, 2018, **19**, 373-378.
33. T.-S. Wu, L.-Y. Syu, B.-H. Lin, S.-C. Weng, H.-T. Jeng, Y.-S. Huang and Y.-L. Soo, *Sci. Rep.*, 2021, **11**, 7668.
34. T.-S. Wu, L.-Y. Syu, C.-N. Lin, B.-H. Lin, Y.-H. Liao, S.-C. Weng, Y.-J. Huang, H.-T. Jeng, S.-Y. Lu, S.-L. Chang and Y.-L. Soo, *Sci. Rep.*, 2019, **9**, 8018.
35. T.-S. Wu, Y. Zhou, R. F. Sabirianov, W.-N. Mei, Y.-L. Soo and C. L. Cheung, *Chem. Commun.*, 2016, **52**, 5003-5006.
36. X. Li, Y. Sun, J. Xu, Y. Shao, J. Wu, X. Xu, Y. Pan, H. Ju, J. Zhu and Y. Xie, *Nat. Energy*, 2019, **4**, 690-699.
37. K. Zhao, J. Qi, H. Yin, Z. Wang, S. Zhao, X. Ma, J. Wan, L. Chang, Y. Gao, R. Yu and Z. Tang, *J. Mater. Chem. A*, 2015, **3**, 20465-20470.
38. C. Canevali, N. Chiodini, F. Morazzoni and R. Scotti, *J. Mater. Chem. C*, 2000, **10**, 773-778.
39. X. Wang, W. Chen, L. Zhang, T. Yao, W. Liu, Y. Lin, H. Ju, J. Dong, L. Zheng, W. Yan, X. Zheng, Z. Li, X. Wang, J. Yang, D. He, Y. Wang, Z. Deng, Y. Wu and Y. Li, *J. Am. Chem. Soc.*, 2017, **139**, 9419-9422.
40. Y. Song, Z. Li, Y. Zhu, X. Feng, J. S. Chen, M. Kaufmann, C. Wang and W. Lin, *J. Am. Chem. Soc.*, 2019, **141**, 12219-12223.
41. F. Xiong, D. Zhou, Z. Xie and Y. Chen, *Appl. Energy*, 2012, **99**, 291-296.
42. A. Kundu, S. K. Dey, S. Dey, A. Anoop and S. Mandal, *Inorg. Chem.*, 2020, **59**, 1461-1470.
43. N. Yuan, X. Gong, W. Sun and C. Yu, *Chemosphere*, 2021, **267**, 128863.
44. X. Yu, Z. Yang, B. Qiu, S. Guo, P. Yang, B. Yu, H. Zhang, Y. Zhao, X. Yang, B. Han and Z. Liu, *Angew. Chem. Int. Ed.*, 2019, **58**, 632-636.
45. R. Shi, H.-F. Ye, F. Liang, Z. Wang, K. Li, Y. Weng, Z. Lin, W.-F. Fu, C.-M. Che and Y. Chen, *Adv. Mater.*, 2018, **30**, 1705941.
46. X. Jiao, X. Li, X. Jin, Y. Sun, J. Xu, L. Liang, H. Ju, J. Zhu, Y. Pan, W. Yan, Y. Lin and Y. Xie, *J. Am. Chem. Soc.*, 2017, **139**, 18044-18051.
47. G. Benkö, J. Kallioinen, J. E. I. Korppi-Tommola, A. P. Yartsev and V. Sundström, *J. Am. Chem. Soc.*, 2002, **124**, 489-493.
48. A. Diguet, N. K. Mani, M. Geoffroy, M. Sollogoub and D. Baigl, *Chem. Eur. J.*, 2010, **16**, 11890-11896.
49. H. Damrauer Niels, G. Cerullo, A. Yeh, R. Boussie Thomas, V. Shank Charles and K. McCusker James, *Science*, 1997, **275**, 54-57.
50. P. Verma, A. Singh, F. A. Rahimi, P. Sarkar, S. Nath, S. K. Pati and T. K. Maji, *Nat. Commun.*, 2021, **12**, 7313.
51. P. Verma, F. A. Rahimi, D. Samanta, A. Kundu, J. Dasgupta and T. K. Maji, *Angew. Chem. Int. Ed.*, 2022, **61**, e202116094.

52. Z. Ma, P. Li, L. Ye, L. Wang, H. Xie and Y. Zhou, *Catal. Sci. Technol.*, 2018, **8**, 5129-5132.
53. L. Liu and Y. Li, *Aerosol Air Qual. Res.*, 2014, **14**, 453-469.
54. Y. Liu, S. Chen, X. Quan and H. Yu, *J. Am. Chem. Soc.*, 2015, **137**, 11631-11636.
55. A. I. Tsiotsias, N. D. Charisiou, I. V. Yentekakis and M. A. Goula, *Catalysts*, 2020, **10**, 812.
56. R. Zhang, H. Wang, S. Tang, C. Liu, F. Dong, H. Yue and B. Liang, *ACS Catal.*, 2018, **8**, 9280-9286.

## Broader context:

Generation of C2-based products from photochemical $CO_2$ reduction reaction ($CO_2$RR) is an important aspect of $CO_2$ valorization toward the formation of high energy density and greater economic value-based product. In that note, $CH_3COOH$ production from $CO_2$ is noteworthy due to the multipurpose utilization in textiles, automobiles, construction, and food additives. Herein, our rational approach of catalyst design by covalent grafting of molecular photosensitizer $[Ru(bpy)_2]^{2+}$ into a defect-based **Ce-MOF** assembly is able to produce $CH_3COOH$ via C-C coupling. Most importantly, the low-lying empty 4f orbitals of $Ce^{4+}$ of **Ce-MOF** boost the electron storage near the catalytic site to enhance the C2 selectivity avoiding C1 product formation. Subsequently, the presence of linker defect in the Ce-oxo cluster resulted in active $CO_2$ binding sites, which enable the facile C-C bond formation via the proximal interaction during the catalysis. Moreover, catalyst is highly stable in water and showed significant activity toward $CH_3COOH$ production. Figuring out the crucial reaction intermediate is the key to unveil the bottleneck of the reaction mechanism. The employment of *in situ* IR study along with DFT calculation has proven crucial to ascertain the key reaction intermediate towards the formation of acetic acid. In addition, the electron transfer pathway is realized from ultrafast transient absorption (TA) spectroscopy and *in situ* UV-Vis spectroscopy. This study provides a transparent insight into efficient C2-based product formation for future advancement through solar-driven MOF-based assembly. Moreover, these findings are encouraging for designing MOF based catalysts towards higher carbon-reduced feedstocks to tackle the energy crisis.

 